

Dynamic optical coherence tomography algorithm for label-free assessment of swiftness and occupancy of intratissue moving scatterers

RION MORISHITA¹, PRADIPTA MUKHERJEE^{1,2}, IBRAHIM ABD EL-SADEK^{1,3}, TANATCHAYA SEESAN^{1,4}, TOMOKO MORI⁵, ATSUKO FURUKAWA⁵, SHINICHI FUKUDA^{6,7}, DONNY LUKMANTO⁶, SATOSHI MATSUSAKA⁵, SHUICHI MAKITA¹, AND YOSHIAKI YASUNO^{1,*}

¹Computational Optics Group, University of Tsukuba, Tsukuba, Ibaraki 305-8573, Japan.

²Centre for Biomedical Engineering, Indian Institute of Technology Delhi, New Delhi-110016, India.

³Department of Physics, Faculty of Science, Damietta University, New Damietta City 34517, Damietta, Egypt.

⁴School of Science, King Mongkut's Institute of Technology Ladkrabang, Bangkok 10520, Thailand.

⁵Clinical Research and Regional Innovation, Faculty of Medicine, University of Tsukuba, Tsukuba, Ibaraki 305-8575, Japan.

⁶Laboratory of Advanced Vision Science, Faculty of Medicine, University of Tsukuba, Tsukuba, Ibaraki 305-8575, Japan.

⁷Department of Ophthalmology, Faculty of Medicine, University of Tsukuba, Ibaraki 305-8575, Japan.

*yoshiaki.yasuno@cog-labs.org

Abstract: Dynamic optical coherence tomography (DOCT) statistically analyzes fluctuations in time-sequential OCT signals, enabling label-free and three-dimensional visualization of intratissue and intracellular activities. Current DOCT methods, such as logarithmic intensity variance (LIV) and OCT correlation decay speed (OCDS) have several limitations. Namely, the DOCT values and intratissue motions are not directly related, and hence DOCT values are not interpretable in the context of the tissue motility. We introduce a new open-source DOCT algorithm that provides more direct interpretation of DOCT in the contexts of dynamic scatterer ratio and scatterer speed in the tissue. The detailed properties of the new and conventional DOCT methods are investigated by numerical simulations based on our open-source DOCT simulation framework, and the experimental validation with *in vitro* and *ex vivo* samples demonstrates the feasibility of the new method.

1. Introduction

Optical coherence tomography (OCT) [1] is a low-coherence interferometric imaging modality, and the advantages of OCT over conventional microscopic techniques have recently led to its use in microscopic investigations [2–11]. First, OCT uses a near-infrared light probe, which provides cellular-level imaging at deeper regions than conventional microscopy, such as at around 1-mm depth. Second, OCT employs the endogenous scattering of the sample as the source of contrast. Hence, OCT is label-free and non-invasive.

One limitation of OCT is its lack of sensitivity to intratissue and intracellular activities. However, this limitation has recently been overcome by an emerging methodology called dynamic OCT (DOCT) [12, 13]. DOCT is a combination of time-sequential OCT signal acquisition and subsequent temporal analysis of the signal sequence.

Several signal analysis algorithms have been developed for DOCT. One type of algorithm computes the variance or standard deviation of the time-sequential OCT signals, directly [12, 14–18] or indirectly [19, 20]. This approach uses the magnitude of the OCT signal fluctuations to contrast intratissue and intracellular activities. Another type of algorithm computes the temporal autocorrelation of time-sequential OCT signals [12, 15, 17], and uses the decorrelation properties as the contrast source. Yet another type of algorithms analyzes the power spectral

density of time-sequential OCT signals through a numerical Fourier transform [21–26], and using the dominant frequency or powers within several frequency bins as the contrast source.

The present authors have previously developed two DOCT algorithms. The first is the logarithmic intensity variance (LIV), which is defined as the time variance of dB-scaled OCT signal intensity [17]. LIV quantifies the magnitude of signal scintillation, which had been considered to related the magnitude of intratissue activities. The other is the OCT correlation decay speed (OCDS), which is defined as the slope of the auto-correlation curve of the time-sequential OCT signal within a particular range of the auto-correlation delay time [17]. OCDS reflects the speed of OCT signal scintillation, which had been considered to relate to the speed of the intratissue activities. Previous studies have examined delay-time ranges of [12.8 ms, 64 ms] and [204.8 ms, 1228.8 ms], with the corresponding OCDS referred to as early OCDS ($OCDS_e$) and late OCDS ($OCDS_l$), respectively [17, 27]. $OCDS_e$ and $OCDS_l$ are considered to be indicators of fast and slow intratissue activities, respectively.

LIV and OCDS have been applied to various biological samples. For tumor spheroids, LIV and OCDS can reveal the alterations in intratissue activities induced by anti-cancer drugs [27–29]. For alveolar organoids, LIV has revealed heterogeneous cellular activities within the alveolar epithelium, which may indicate abnormal reprogramming of the epithelial cells, a phenomenon known as bronchiolization [30]. For *ex vivo* mouse organs, LIV has revealed metabolic activities in livers [31, 32] and kidneys [33]. LIV has also been successfully applied to *in vivo* human skin, *in vitro* skin models, and *ex vivo* skin samples [34].

Despite their feasibility and utility, the LIV and OCDS algorithms have two shortcomings. First, OCDS is not a direct indicator of the speed of dynamics. The selection of the delay-time range is arbitrary, and the correlation decay slope within a specific delay range neither directly nor monotonically correlates with the speed of the dynamics. Second, these DOCT methods quantify the dynamics of OCT signals rather than the dynamics of tissues. The relationship between the OCT-signal dynamics and tissue dynamics remains unclear. These two shortcomings hinder the interpretation of LIV and OCDS images in the context of tissue activities.

This paper addresses these two issues. The first issue is solved by introducing two new DOCT metrics (i.e., contrasts), which are computed simultaneously from an OCT time sequence. The first metric, “Swiftness”, is a more direct indicator of the speed of tissue dynamics than OCDS. The second metric, “authentic LIV (aLIV)”, is a byproduct of Swiftness, and provides an alternative to LIV. The second issue is solved by numerically analyzing the relationship between tissue dynamics and various DOCT metrics, including LIV, OCDS, Swiftness, and aLIV. For the numerical simulations, we conduct a mathematical model of dynamic tissues as an extension of our previous dispersed scatterer model (DSM) [35]. Briefly, this paper consists of three main components: the principles of the new DOCT metrics (Section 2), a numerical study investigating their properties (Section 3), and an experimental study validating their applicability to biological samples (Section 4). For the experimental study, *in vitro* tumor spheroids and an *ex vivo* mouse kidney are used as samples.

2. New DOCT algorithm

Our new open-source DOCT algorithm [36] uses the dependency of conventional LIV on the size of the acquisition-time-window (A_{tw}) [17]. LIV is defined as the time variance of the time-sequential OCT signal. Thus, LIV becomes larger or smaller in proportion to the fluctuation magnitude of the OCT signal. However, LIV is also influenced by the size of A_{tw} ; specifically, LIV (i.e., the time variance) inevitably decreases as A_{tw} becomes smaller.

Figure 1 schematically illustrates the properties of LIV, where curves A, B, and C represent the cases of faster, moderate, and slower signal fluctuations, respectively. LIV increases as A_{tw} becomes larger, and then saturates when A_{tw} is sufficiently large in respect to the signal fluctuation cycle.

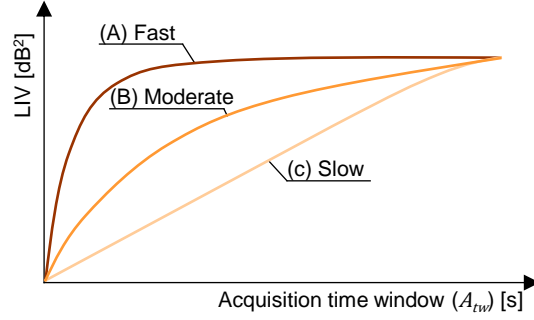


Fig. 1. Schematic illustrating the acquisition-time-window (A_{tw})-size dependency of LIV. LIV inevitably decreases as A_{tw} becomes smaller. Curves A, B, and C represent the cases of faster, moderate, and slower signal fluctuations, respectively.

In this paper, we propose new DOCT metrics (contrasts) by leveraging this property of LIV. One metric, related to the speed of intratissue activity, is defined from the salutation speed of the LIV- A_{tw} curve. The other metric, quantifying the magnitude of OCT signal fluctuations, is defined by the saturation level of the curve. The theory and algorithm are described in detail in the following sections.

2.1. LIV curve

In the new DOCT method, similar to conventional DOCT imaging, OCT frames are repeatedly acquired with a time interval of Δt over A_{tw} at the same sample location, as schematically illustrated in (i, red box) of Fig. 2.

Several LIV values with different time window are then computed to form the LIV- T_w curve. For this computation, at first, data subsets of different time window (T_w) sizes are extracted from the time-sequential OCT signal [(ii) of Fig. 2]. For clarification, the total acquisition time duration for the time-sequential OCT signal is the acquisition time window (A_{tw}), while the time duration of each data subset used to compute an LIV value is the time window (T_w).

Subsequently, as illustrated in (iii) of Fig. 2, the LIV values of each data subset are calculated in the same way as for conventional LIV [17, 27], i.e.,

$$\text{LIV}(x, z) = \frac{1}{N} \sum_{i=0}^{N-1} [\text{I}_{\text{dB}}(x, z, t_i) - \langle \text{I}_{\text{dB}}(x, z, t_i) \rangle_t]^2, \quad (1)$$

where $\text{I}_{\text{dB}}(x, z, t_i)$ represents the dB-scaled OCT signal intensity at a depth of z and a lateral position of x in the OCT frame. t_i is the sampling time of the i -th OCT frame, where $i = 0, 1, 2, \dots, N-1$, and N is the total number of frames in the data subset. $\langle \rangle_t$ denotes averaging over time. The smallest T_w corresponds to the inter-frame interval $\Delta t = t_i - t_{i-1}$ of the time-sequential OCT frames, while the largest T_w is equal to A_{tw} .

Note that two or more data subsets with identical T_w can be obtained, except for the largest T_w . In the cases where multiple data subsets share the same T_w , the LIV values for all subsets are computed and then averaged [(iv) of Fig. 2] as

$$\overline{\text{LIV}}(x, z; T_w) = \frac{1}{N_{T_w}} \sum_{l=0}^{N_{T_w}-1} \text{LIV}_l(x, z; T_w), \quad (2)$$

where $\overline{\text{LIV}}(x, z; T_w)$ is the averaged LIV for a specific T_w and $\text{LIV}_l(x, z; T_w)$ represents the l -th LIV among all LIV values with identical T_w , where $l = 0, 1, 2, \dots, N_{T_w} - 1$. N_{T_w} represents

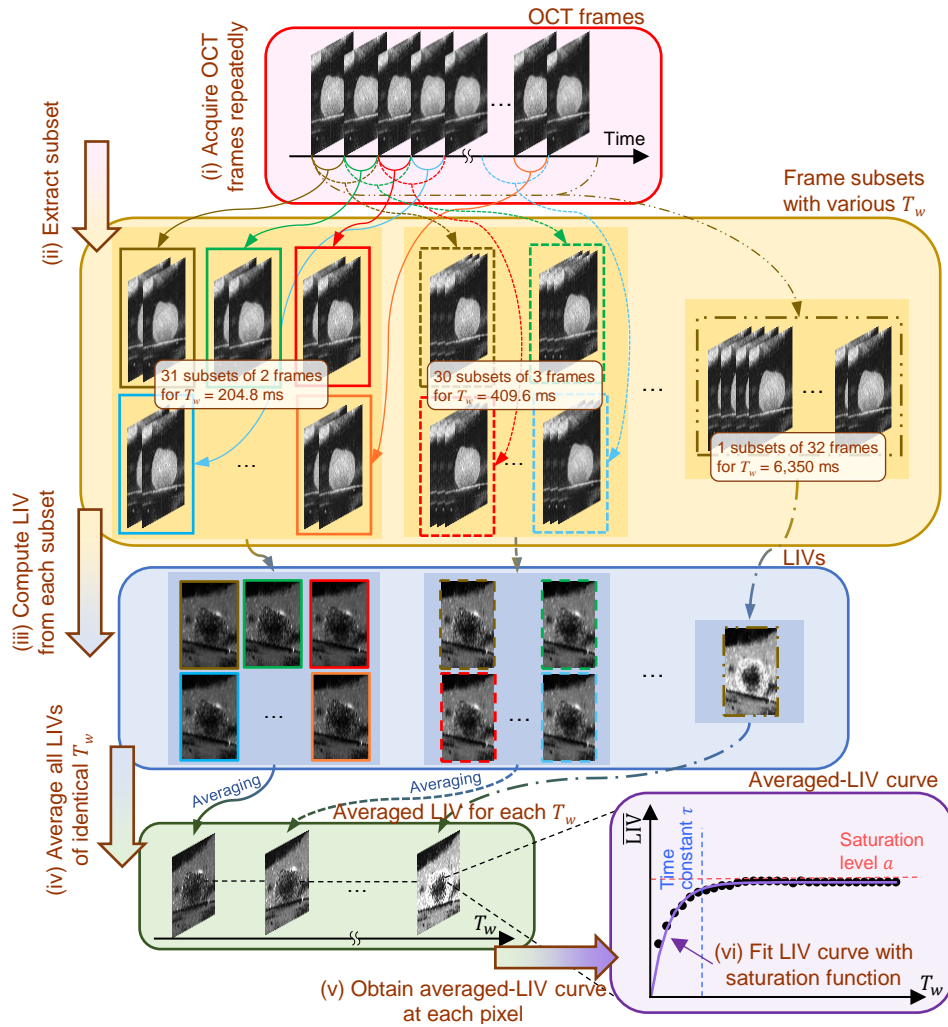


Fig. 2. Diagram showing the principle of the new DOCT algorithm. (i) OCT frames are repeatedly acquired with a time interval of Δt over A_{T_w} . (ii) All combinations of data subsets are extracted for different time window (T_w) sizes from the time-sequential OCT frames. (iii) LIV is computed from each data subset. (iv) All LIV values with identical T_w are averaged. (v) A curve of the averaged LIV over T_w is obtained, which is referred to as the "LIV curve". (vi) The LIV curve is fitted with a first-order saturation function of T_w .

the total number of LIV values corresponding to identical T_w . This averaged LIV is used as the representative LIV of that particular time window.

The averaged LIVs are computed for all possible T_w values and, at each pixel, a curve of the averaged LIV is obtained as a function of T_w , as schematically depicted in (v) of Fig. 2. This curve of the averaged LIV over T_w is hereafter referred to as the ‘‘LIV curve’’.

2.2. Authentic LIV and Swiftness

To extract the characteristic parameters, the LIV curve obtained using the method described in Section 2.1, i.e., the curve of the averaged LIV along T_w at each pixel, is fitted with a first-order saturation function of T_w [(vi) in Fig. 2]:

$$f_{\text{LIV}}(T_w; a, \tau) = a [1 - \exp(-T_w/\tau)], \quad (3)$$

where the fitting parameters a and τ represent the saturation level and the time constant, respectively.

We define two DOCT metrics using these fitting parameters. The first metric is the ‘‘authentic LIV (aLIV),’’ which is defined as

$$\text{aLIV} \equiv a. \quad (4)$$

In principle, aLIV is expected to be an A_{T_w} -independent version of LIV.

The second metric, ‘‘Swiftness,’’ is defined as

$$\text{Swiftness} \equiv \frac{1}{\tau}. \quad (5)$$

Swiftness quantifies the saturation speed of the LIV curve.

It should be noted that both aLIV and Swiftness are direct measures of the fluctuation of the OCT signal, rather than the intratissue dynamics. The relationships between the intratissue dynamics and these DOCT metrics will be discussed in Section 3.

2.3. Implementation of aLIV and Swiftness

In our implementation, the new DOCT algorithm is applied to OCT frames that are acquired 32 times with an inter-frame time of 204.8 ms (see Section 4.1.2 for details). Namely, the smallest T_w is 204.8 ms (corresponding to the two-frame subsets) and the largest T_w is 6.3 s (corresponding to the 32-frame subset).

To improve the accuracy of fitting the LIV curve, the LIV curve is smoothed by applying 3×3 kernel averaging to each averaged LIV cross-section $\overline{\text{LIV}}(x, z; T_w)$ at each T_w . The kernel averaging is implemented using the OpenCV function ‘‘cv2.blur()’’.

For the function fitting, the Levenberg-Marquardt algorithm is used to solve the nonlinear least-squares problem. The first-order saturation function in Eq. (3) is used as the model function and the optimal values of a and τ within the range $[0, \infty]$ are determined.

The processing for the new DOCT algorithm was executed on a laptop PC equipped with an Intel Core i7-10750H CPU and 32 GB memory, running the Windows 10 Pro operating system. The PC was also equipped with a graphic processing unit (GPU), specifically NVIDIA GeForce RTX 2070 Super with Max-Q Design.

The new DOCT algorithm was implemented in Python 3.8.5 using NumPy 1.19.2 and CuPy 10.0.0 libraries for all computations except function fitting. To accelerate the function fitting, the GPU and an open-source GPU-accelerated implementation of function fitting (Gpufit [37]) were used. The LIV curve was fitted using the ‘‘gf.fit_constrained()’’ function in the Gpufit 1.2.0 library. The first-order saturation function [Eq. (3)] is not included in the built-in model functions of Gpufit library. Thus, we implemented the function module and recompiled the library with this module. The Python implementation of the new DOCT algorithm is available as open source at the GitHub repository [36]. Details regarding the processing time are discussed in Section 5.3.

3. Numerical investigation of DOCT properties

The relationships between the intratissue dynamics and DOCT metrics were investigated through numerical simulations using our open-source DOCT simulation framework [38].

3.1. Simulation theory and method

3.1.1. Dynamic sample modeling

We modeled a sample based on dispersed scatterer model (DSM) [35], which represents a sample as a spatially slowly varying refractive index distribution with infinitely small scatterers randomly dispersed throughout the sample. In our simulations, the slowly varying refractive indices were simplified to be constant, and the refractive indices of all the scatterers were assumed to be identical. Hence, the all scatterers had the same intensity reflectivity. It should be noted that the sample represented by this model does not have macroscopic inhomogeneity (i.e., large structure). However, each DOCT value is computed from a small region, as small as the size of the point spread function (PSF) of OCT. And hence, this lack of large structure is not a significant limitation of the simulation.

The intratissue scatterers were assumed to follow not Brownian motion (i.e., diffusion) but random ballistic motion in which all scatterers move rectilinearly with the same constant speed v , but with a motion direction that is randomly chosen. This selection of random ballistic motion was based on an extensive literature survey about the intratissue and intracellular activities [39]. Further points about the motion model will be discussed in Section 5.5. Assuming the initial position of the j -th scatterer is (x_{j0}, y_{j0}, z_{j0}) , the three-dimensional (3D) position of the scatterer after a particular travel time t is given by

$$\begin{aligned} x_j(t; \varphi_j, \theta_j) &= x_{j0} + vt \sin \varphi_j \cos \theta_j, \\ y_j(t; \varphi_j, \theta_j) &= y_{j0} + vt \sin \varphi_j \sin \theta_j, \\ z_j(t; \varphi_j, \theta_j) &= z_{j0} + vt \cos \varphi_j, \end{aligned} \quad (6)$$

where φ_j and θ_j are the azimuth and inclination angles, respectively, of the j -th scatterer's motion. The position of the j -th scatterer at the i -th time point is expressed in incremental form as

$$\begin{aligned} x_j(t_i; \varphi_j, \theta_j) &= x_j(t_{i-1}; \varphi_j, \theta_j) + v\Delta t \sin \varphi_j \cos \theta_j, \\ y_j(t_i; \varphi_j, \theta_j) &= y_j(t_{i-1}; \varphi_j, \theta_j) + v\Delta t \sin \varphi_j \sin \theta_j, \\ z_j(t_i; \varphi_j, \theta_j) &= z_j(t_{i-1}; \varphi_j, \theta_j) + v\Delta t \cos \varphi_j, \end{aligned} \quad (7)$$

where $\Delta t = t_i - t_{i-1}$ is the time interval between successive time points.

In the analyses in Sections 3.2 and 3.3, we investigate the situation where dynamic scatterers and static scatterers coexist. In this case, a portion of the scatterers move according to Eq. (6) (or equivalently according to Eq. (7)), while the other scatterers do not move.

3.1.2. DOCT signal modeling

At a single point in an image, the complex OCT signal obtained from the modeled sample is expressed as a summation of electric field contributions from each scatterer as

$$\begin{aligned} E(t) \propto \sum_{j=0}^{N_s-1} b_j \exp \left[i \frac{2\pi}{\lambda} 2z_j(t) + i \frac{2\pi}{\lambda} 2\Delta z \right] \\ \exp \left[-\frac{1}{2} \left(\frac{x_j(t)}{\sigma_x} \right)^2 - \frac{1}{2} \left(\frac{y_j(t)}{\sigma_y} \right)^2 - \frac{1}{2} \left(\frac{z_j(t)}{\sigma_z} \right)^2 \right], \end{aligned} \quad (8)$$

where j is the scatterer index and N_s is the number of scatterers in the sample. The term b_j and the first exponential part (green part) correspond to the complex reflectivity of the j -th scatterer. Here, b_j is a coefficient accounting for the different reflectivity values of the scatterers, and we assume that this is 1 for all scatterers. The exponential part represents the phase defined by the depth position of the scatterer, where λ is the center wavelength of the probe beam and Δz is the path length offset, defined by the arm lengths of the interference. Δz is a constant for all scatterer contributions, and therefore it does not affect the intensity of the OCT signal.

The second exponential (red) represents the 3D Gaussian PSF centered at $(x, y, z) = (0, 0, 0)$, and (x_j, y_j, z_j) is the position of the j -th scatterer. Namely, the contributions from each scatterer are weighted by the PSF. Let σ_x , σ_y , and σ_z denote the width of the amplitude PSF defined by the standard deviation of the Gaussian. The standard deviation and the $1/e^2$ width and full width at half maximum (FWHM) of the intensity of the OCT signal are related according to

$$\begin{aligned}\sigma &= \frac{1}{2\sqrt{2}}w_e, \\ \sigma &= \frac{1}{2\sqrt{\ln 2}}w_{\text{FWHM}},\end{aligned}\tag{9}$$

where σ is the standard deviation width of the amplitude PSF and w_e , w_{FWHM} are the $1/e^2$ width and FWHM of the OCT signal intensity, respectively.

Finally, the intensity of the OCT signal is obtained as

$$I(t) = E(t)E^*(t),\tag{10}$$

where $*$ denotes the complex conjugate.

3.1.3. Numerical generation of OCT time sequence

The time sequence of the OCT intensity signal at a single point in the image is numerically simulated based on the theories described in Sections 3.1.1 and 3.1.2.

Specifically, we first generated a 3D numerical analysis field and randomly seeded the scatterers in the field. As stated in Section 3.1.1, we assumed that all scatterers had the same speed $|v|$, but random motion directions. We computed the complex OCT signal at a single position in the image from the numerical field using Eq. (8), and then computed the OCT intensity from Eq. (10). After computing the OCT intensity at a time point, the positions of the scatterers were updated based on Eq. (7), and the OCT intensity at the new time point was computed. By repeating this process, the time sequence of OCT intensity at a single position in an image was obtained.

A scatterer that enters the analytic field during the simulation time, but had an initial position outside the analytic field, would not have been numerically seeded, and hence, would not contribute to the simulation results. This reduces the simulation accuracy. To lessen the effect of this inaccuracy, the length of the 3D analysis field is set to be $5\sigma_{\{x,y,z\}} + 2|v|A_{tw}$ for each direction, where the subscript $\{x, y, z\}$ corresponds to one of x , y , or z . Namely, the field extends for 5σ -width of the complex PSF plus the maximum travel distance of a scatterer at both sides (see Supplementary Fig. S1 for schematic depiction).

The OCT system parameters used for the simulations are identical to those of the OCT device used in the experimental validation described in Section 4, i.e., $\lambda = 1.3 \mu\text{m}$, the lateral resolution is $18 \mu\text{m}$ ($1/e^2$ -width of intensity), and the axial resolution is $14 \mu\text{m}$ (FWHM). The time-sequential OCT intensity was generated with a time interval (i.e., OCT frame interval) of 204.8 ms for 32 time points, therefore, $A_{tw} = 6.35 \text{ s}$, i.e., $204.8 \text{ ms} \times (32 - 1)$. These parameters are consistent with the experiment described in Section 4.1.2.

3.1.4. Computation of DOCT values

Four DOCT metrics, including the proposed aLIV and Swiftness metrics and our conventional LIV and OCDS metrics, were computed from the simulated time sequence of OCT intensity.

The proposed aLIV and Swiftness metrics were computed following the method described in Section 2. In the simulations, nine LIV curves were averaged before performing the LIV curve fitting to emulate the 3×3 -spatial-kernel averaging, which is one of the processing procedures explained in Section 2.3.

The conventional metrics of LIV and OCDS were computed using the method described in Ref. [17,27]. Namely, the time variance of the dB-scaled OCT intensity [Eq. (1)] was computed as the LIV, while the slope of the auto-correlation function of the dB-scaled OCT intensity at a delay-time range of [204.8 ms, 1228.8 ms] was computed as OCDS. This delay-time range is the same as that of $OCDS_l$ in Ref. [27], and $OCDS_l$ is known to be sensitive to relatively slow activity. In the simulations, LIV and OCDS were obtained by averaging nine LIV and OCDS values to maintain consistency with the 3×3 -kernel averaging in the aLIV and Swiftness computations.

It should be noted that, in real measurements (i.e., experiments), DOCT signals can be affected by fluctuations in the superior tissues, similar to the well-known projection artifact in OCT angiography [40]. This effect is not accounted for in our simulation. Since the purpose of the simulation is to clarify the relationship between the DOCT signals and the local motion of the sample, this omission is not a significant limitation.

3.2. Numerical study protocol

We conducted two numerical studies. One investigated the dependencies of the DOCT metrics on the scatterer speed, while the other examined the dependency of the DOCT metrics on the proportion of dynamic scatterers. The study protocols are described in the following subsections.

In addition to the newly introduced metrics (i.e., aLIV and Swiftness), previously established metrics, including LIV and OCDS, were also incorporated in each study. This is because several *in vitro* and *ex vivo* samples have been analyzed using LIV and OCDS, with many carefully interpreted through comparisons with standard histology and fluorescence micrographs. Comparing the new and existing DOCT metrics may facilitate the interpretation of images obtained using the newly introduced metrics.

3.2.1. Study 1: Scatterer-speed dependency

The first study investigated the scatterer-speed dependency of the DOCT metrics. The simulations were conducted for 200 different scatterer speeds, selected from a range of [1.0 nm/s, 6.0 $\mu\text{m/s}$]. These 200 different speeds were not equally spaced, but were selected to clearly highlight the characteristics of the speed dependency. The minimum speed of the range (1.0 nm/s) was selected to cover the practical speed range of intratissue/intracellular motions which is from around 10 nm/s to 10 $\mu\text{m/s}$ [39,41]. Although the maximum speed of the simulation (6.0 $\mu\text{m/s}$) is slower than the maximum speed in the practical tissues/cells (10 $\mu\text{m/s}$), it results in a total displacement of 37.8 μm over the simulation time window of 6.3 s, which is slightly larger than twice the lateral resolution of 18 μm . And hence, the selected speed range is reasonable. The speed was the same for all scatterers, but the direction of each scatterer was randomly selected.

The scatterer density was set to 0.055 scatterers/ μm^3 based on previously measured scatterer densities of tumor spheroids using a neural-network-based scatterer density estimator (NN-SDE) [42,43]. The NN-SDE is a NN model that processes a local OCT speckle pattern and estimates the scatterer density of the sample. Both in the present numerical simulation and in the principle of the NN-SDE, the scatterer density is interpreted as the “density of effective scatterers,” where the effective scatterer is the scatterer whose scattering contributes to the OCT signal.

From the simulated time sequence of OCT intensity at each speed, the four DOCT metrics of aLIV, Swiftness, LIV, and OCDS were computed. For each speed, five simulation trials were performed, and the median of each DOCT metric was used as the result.

3.2.2. Study 2: Dynamic-scatterer ratio dependency

In the second study, we assumed that a portion of the scatterers exhibit random ballistic motion, while the other scatterers remain static, i.e., not moving. The dependency of the DOCT metrics on the dynamic scatterer ratio was investigated.

The dynamic-scatterer ratio (DSR) is defined as

$$\text{DSR} = \frac{\text{Number of dynamic scatterers}}{\text{Total number of scatterers}}. \quad (11)$$

Simulations were conducted for 100 equally distributed DSRs in the range [0.0, 1.0]. The scatterer density was set to the same as that of Study 1, i.e., $0.055 \text{ scatterers}/\mu\text{m}^3$. The total number of scatterers and the scatterer density were held constant regardless of the DSR.

The DSR dependency of aLIV, Swiftness, LIV, and OCDS was investigated for dynamic scatterer speeds of 0.01, 0.05, 0.1, 0.2, 0.6, and $3 \mu\text{m/s}$. Similar to Study 1, five simulation trials were conducted for each DSR, and the median among the five trials was taken as the result.

3.3. Results of numerical validation

3.3.1. Study 1: Scatterer-speed dependency

Figure 3(a, c, e, g) shows the scatterer-speed dependency of aLIV, LIV, Swiftness, and OCDS.

Both aLIV and LIV remain constant at around 30 dB^2 for higher scatterer speeds [Fig. 3(a, c)], which is consistent with the maximum LIV values reported in previous *ex vivo* and *in vitro* studies [29–32]. For slower scatterer speeds, where $|v| < 0.2 \mu\text{m/s}$, LIV becomes smaller as the scatterer speed decreases. In contrast, aLIV becomes extremely large and extends beyond the plot region. This is because the LIV curve cannot be correctly fitted for very slow scatterer speeds. This issue is extensively discussed in Section 5.2.

Swiftness exhibits saturation with respect to the scatterer speed [Fig. 3(e)], except for some minor oscillations. Namely, Swiftness increases monotonically as the scatterer speed increases up to around $1.2 \mu\text{m/s}$, and then remains at around 2.5 s^{-1} at higher scatterer speeds. Thus, Swiftness can be considered to be sensitive to scatterer speeds if it is less than $1.2 \mu\text{m/s}$.

OCDS exhibits a pinnacle that peaks around $0.1 \mu\text{m/s}$ [Fig. 3(g), magnified in the inset]. This indicates that OCDS is sensitive to a specific speed range. This is advantageous because it allows OCDS to be used as a fingerprint for detecting a particular speed. It is noteworthy that the fingerprint speed zone can be customized by adjusting the delay-time range used to fit the slope of the auto-correlation function.

The minor oscillations observed in Swiftness and other unexplained observations will be examined as part of an ongoing comprehensive numerical investigation of DOCT [39, 44].

3.3.2. Study 2: DSR dependency

Figure 3(b, d, f, h) shows the dependency of aLIV, LIV, Swiftness, and OCDS on DSR.

Both aLIV and LIV increase monotonically with increasing DSR [Fig. 3(b, d)] when the scatterer speed is greater than $0.2 \mu\text{m/s}$. However, when the speed of the dynamic scatterers is less than $0.1 \mu\text{m/s}$, aLIV diverges to extremely large values. For speeds slower than $0.05 \mu\text{m/s}$, almost all aLIV values were plotted outside of the plot region. In contrast, LIV become smaller with decreasing scatterer speed, as shown in Fig. 3(d).

This property of LIV makes it difficult to estimate the DSR from the LIV value, namely, one value of LIV can correspond to multiple DSRs at different scatterer speeds. In contrast, aLIV becomes extremely large and is unreliable when the scatterer speed is slow. The unreliable values

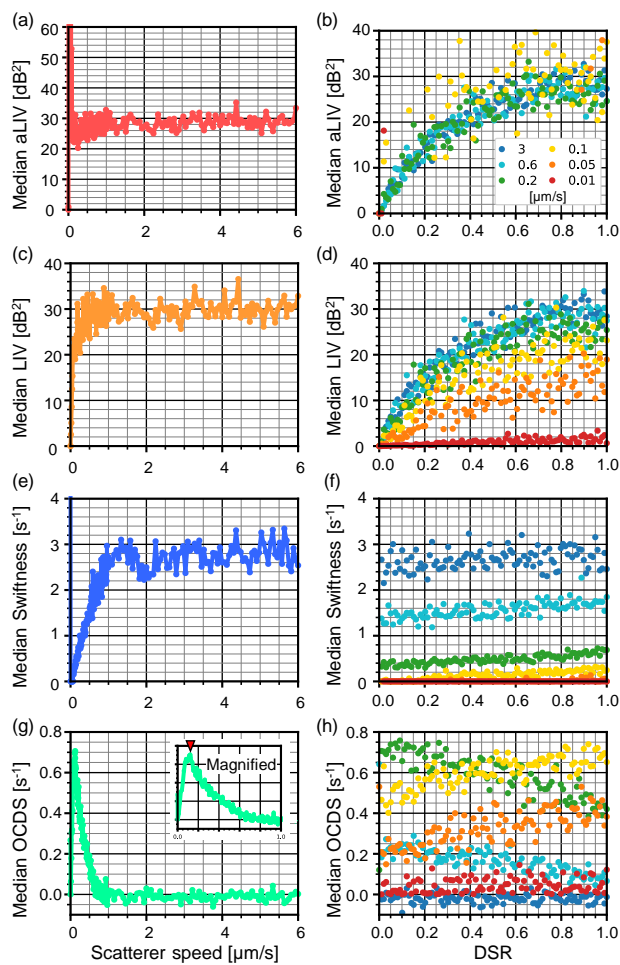


Fig. 3. The scatterer-speed dependencies (a, c, e, g) and dynamic-scatterer-ratio (DSR) dependencies (b, d, f, h) of aLIV, LIV, Swiftness, and OCDS obtained by numerical simulations. The point colors of the DSR-dependency plots indicate the speed of the dynamic scatterers as shown in the legend in (b). In the magnified plot for the speed range $[0, 1 \mu\text{m/s}]$ (g), the peak location of OCDS is indicated with the arrowhead.

of aLIV can be automatically detected and removed, as discussed in Section 5.2. For cases where aLIV is not divergent, nearly identical aLIV-DSR curves are observed for all dynamic scatterer speeds [Fig. 3(b)], indicating a one-to-one relationship between aLIV and DSR. Hence, the aLIV value is specific to a certain DSR value in the range where the aLIV value is reliable.

Swiftness shows a slight increase with increasing DSR [Fig. 3(f)], but the impact of DSR on Swiftness is significantly smaller than that of the scatterer speed.

OCDS shows either a monotonic increase or decrease with respect to changes in DSR. A monotonic increase occurs [warm-color plots, Fig. 3(h)] when the dynamic scatterer speed is slower than the fingerprint peak speed observed in Fig. 3(g). Conversely, a monotonic decrease occurs [cool-color plots, Fig. 3(h)] when the dynamic scatterer speed is faster than the fingerprint peak speed. The slope of OCDS with respect to DSR becomes steeper as the dynamic scatterer speed moves closer to the fingerprint peak in Fig. 3(g). However, the change in OCDS with respect to DSR in Fig. 3(h) is much smaller than the response to the fingerprint speed in Fig. 3(g). Therefore, the conclusion of Study 1, namely, that OCDS can be used as a fingerprint for a particular speed, is still supported.

3.4. Summary of DOCT metrics' properties

The numerical simulations have demonstrated that aLIV is sensitive to the DSR, such that aLIV becomes larger for higher values of DSR, in the range where the aLIV value is reliable. In addition, unreliable aLIV values can be automatically detected (Section 5.2). Therefore, aLIV can be used as an indicator of the dynamic scatterer ratio (i.e., the occupancy of the dynamic scatterers).

LIV also exhibits sensitivity to DSR, similar to aLIV. However, as shown in Fig. 3(d), it is difficult to determine a unique DSR from the LIV value if the scatterer speed is unknown.

Swiftness increases almost monotonically as the scatterer speed increases, especially for speeds of less than 1.2 $\mu\text{m/s}$. In addition, Swiftness is relatively insensitive to DSR. Thus, Swiftness can be used as an indicator for the speed of dynamic scatterers. It is noteworthy that, although the monotonic relation can be found only up to 1.2 $\mu\text{m/s}$, this maximum speed of the monotonic relation can be enlarged by using a shorter interval of OCT frame acquisition.

OCDS displays a distinct peak at a particular scatterer speed, indicating that this metric can be used as a fingerprint for a specific scatterer speed. The principle of OCDS suggests that the fingerprint speed zone can be selected by changing the delay-time range. Furthermore, the location and width of the fingerprint speed zone can be identified from numerical simulations.

4. Experimental validation of new DOCT metrics

To assess the applicability of aLIV and Swiftness to biological samples, we imaged *in vitro* tumor spheroids and *ex vivo* mouse kidney samples.

4.1. Method of experimental validation

4.1.1. Samples

Four tumor spheroids treated with an anti-cancer drug were involved. The tumor spheroids were formed with human breast cancer cells (MCF-7 cell line) in each well of a 96-well plate under a cultivation environment. Three of the four spheroids were treated with 1- μM paclitaxel (PTX) for 1, 3, and 6 days, respectively, while the remaining spheroid was untreated.

After drug treatment, each spheroid was measured using an OCT microscope. The cultivation and measurement protocols have been detailed elsewhere in Ref. [28], and the raw data used in the present study are identical to those presented in this reference.

An *ex vivo* C57BL/6 healthy mouse kidney was also examined in this study. The sample preparation has been described elsewhere in Ref. [33], and the raw OCT data presented in Fig. 1

of this reference was used in this study.

The mouse kidney experiments were performed in accordance with the animal study guidelines of the University of Tsukuba. All experimental protocols were approved by the Institutional Animal Care and Use Committee (IACUC) of the University of Tsukuba. The present study was designed, performed, and reported according to Animal Research: Reporting of *In vivo* Experiments (ARRIVE) guidelines. The raw OCT data of Ref. [33] was used, and thus no additional animal experiments were conducted for the present validation.

4.1.2. OCT microscope and DOCT measurement

A custom-made Jones-matrix swept-source OCT microscope with a scan speed of 50,000 A-lines/s was used for the measurements. This OCT microscope has a probe beam center wavelength of 1.3 μm and resolutions of 18 μm ($1/e^2$ width) and 14 μm (FWHM in tissue) for the lateral and axial directions, respectively. Although this OCT microscope is polarization sensitive, the DOCT imaging did not use polarization information. The polarization-insensitive OCT intensity signal was obtained by averaging linear intensities of four OCT images acquired from four different polarization channels. The OCT system is described in detail elsewhere [45, 46].

Time-sequential OCT data were acquired using a repeating raster scan protocol [27]. The transversal fields of view (FOVs) were 1 mm \times 1 mm for the tumor spheroids and 6 mm \times 6 mm for the mouse kidney. The *en face* FOV was divided into eight sub-fields along the slow scan direction, with each sub-field consisting of 16 B-scan locations. The raster-scan was performed 32 times for each sub-field. As a result, a time series of 32 frames was acquired at each B-scan location. The inter-frame time was 204.8 ms and the time separation between the first and last frames was 6.35 s. Each frame comprised 512 A-lines.

For DOCT imaging, aLIV and Swiftness were computed as described in Section 2. LIV and OCDS were computed by the method described in Section 3.1.4. We applied 3 \times 3-pixel kernel averaging in the cross-sectional plane to each of the LIV and OCDS images. The pseudo-color DOCT images were generated using the OCT intensity and the DOCT as the pixel brightness and hue, respectively.

4.1.3. Study design and protocol

We conducted two studies. In Study 1, the image appearances were subjectively compared between four types of DOCT images (i.e., aLIV, Swiftness, LIV, and OCDS). We also used fluorescence images for the biological interpretation of the tumor spheroids.

In Study 2, we investigated the impact of A_{tw} on the DOCT metrics and the image appearances. To examine the effect of A_{tw} , we virtually shortened A_{tw} by truncating the frame sequence, which initially contained 32 frames. Here, the virtually shortened A_{tw} is referred to as the virtual acquisition time window ($\mathcal{V}A_{tw}$). Six different $\mathcal{V}A_{tw}$ were investigated, i.e., $\mathcal{V}A_{tw} = 0.41, 1.23, 2.46, 3.69, 4.91, \text{ and } 6.35$ s. The time-sequential OCT data for each $\mathcal{V}A_{tw}$ consisted of a different number of frames, i.e., 3, 7, 13, 19, 25, and 32 frames.

Quantitative metrics-for-comparison were calculated from two regions of interest (ROIs) in the untreated spheroid. The ROIs were manually defined as shown in Fig. 6(e). It is known that the spheroids have two domains, a necrotic core and a vital periphery. Each domain exhibits different DOCT values and is mostly homogeneous. Thus, each ROI was defined in core and periphery regions.

We computed two types of metrics including the average DOCT value at each ROI, and the contrast between the core and periphery ROIs defined as

$$C = \frac{|M_c - M_p|}{M_c + M_p}, \quad (12)$$

where M_c and M_p represent the average values in the core and periphery ROIs, respectively.

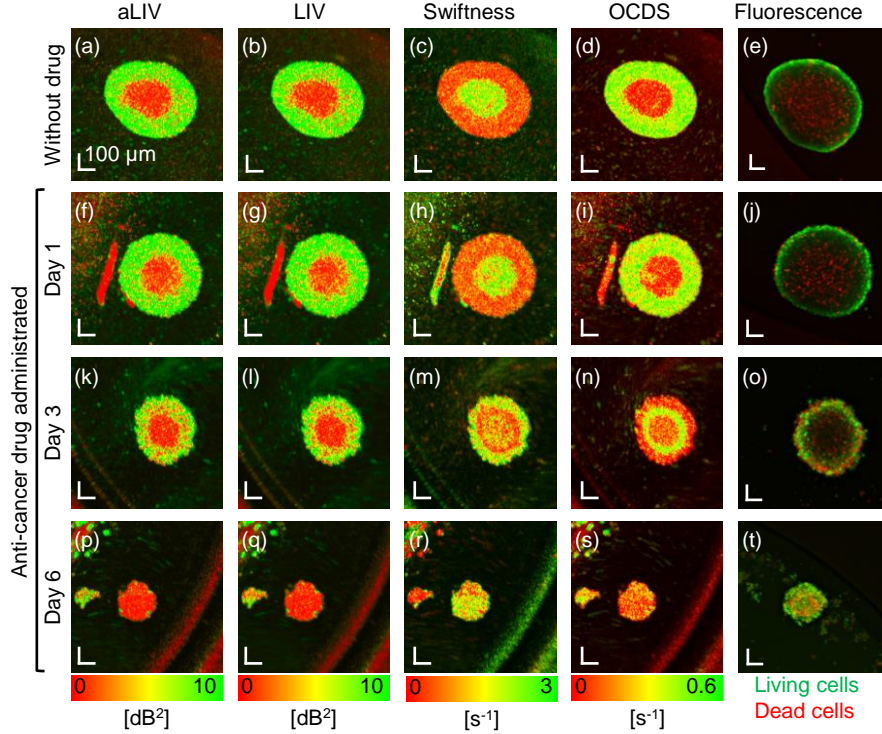


Fig. 4. The *en face* aLIV, LIV, Swiftness, OCDS, and fluorescence images of the tumor spheroids treated by the anti-cancer drug (1- μ M PTX) for 1, 3, and 6 days. The scale bars represent 100 μ m. In the region with high aLIV (green), the dynamic scatterer ratio is expected to be high, while in the region with high Swiftness, the dynamic scatterers are expected to move rapidly.

Some pixels produced unreliable aLIV and Swiftness values because of the low fitting accuracy of the LIV curve. These pixels were detected automatically and excluded from the averaging. Details of the unreliable pixels and their automatic detection are described in Section 5.2.

It should be noted that the protocol of Study 2 is suboptimal, as the number of frames varies among the VA_{TW} configurations. However, the effect of varying frame numbers is negligible for the following reasons. Specifically, all four types of DOCT metrics are derived from the variance of OCT signals. OCDS, in particular, is calculated from the correlation coefficient, which is defined using variances and covariance. As is well known in statistical theory, the expected value of variance is not significantly affected by the number of data points.

The mouse kidney was not used in Study 2, because it did not contain simple large-domain structures.

4.2. Results

4.2.1. Study 1

Figure 4 presents the *en face* aLIV, LIV, Swiftness, OCDS, and fluorescence images (from left to right) of the untreated (1st row) and anti-cancer (1- μ M PTX) drug-treated tumor spheroids (treatment for 1, 3, and 6 days shown in 2nd, 3rd, and 4th rows, respectively). The fluorescence images were captured using a wide-field fluorescence microscope (THUNDER imager DMi8; Leica Micro-systems, Wetzlar, Germany) with a microscopic objective lens (numerical aperture

of 0.12). Living cells were highlighted with calcein-acetoxymethyl (calcein-AM; Dojindo, Kumamoto, Japan), which emits a green fluorescence signal, while dead cells were highlighted with propidium iodide (PI; Dojindo), which emits a red fluorescence signal.

For the without-drug and 1-day-treated spheroids, a concentric pattern consisting of two zones is observed in both the DOCT and fluorescence images [Fig. 4(a–j)]. The fluorescence images show dead cells (red) concentrated in the inner zone, while living cells (green) are distributed in the periphery. These characteristics are consistent with the well-known necrotic core formation of MCF-7 spheroids [47], which is caused by hypoxia and nutrient deficiency in the central region. Therefore, the inner and outer zones of the concentric pattern in the DOCT images may also correspond to the necrotic core and the living cells, respectively.

The inner zone, i.e., necrotic core, exhibits low aLIV, low LIV, high Swiftness, and low OCDS. According to the simulation results, the DOCT contrast indicates that only a small proportion of scatterers within the necrotic core are dynamic (as suggested by the low aLIV and LIV), but these dynamic scatterers move rapidly (as suggested by the high Swiftness). The speed of the dynamic scatterers is outside the sensitive range, i.e., fingerprint speed zone, of OCDS (as suggested by the low OCDS, see Section 3.3.1). The Swiftness values further confirm that the speed exceeds the fingerprint speed zone of OCDS. In contrast, the outer zone, i.e., spheroid periphery, contains a large proportion of dynamic scatterers (high aLIV and LIV), but these dynamic scatterers move slowly (low Swiftness) and their speed is within the fingerprint speed zone of OCDS, resulting in the high OCDS value.

For the 3-day-treated spheroid, the Swiftness and OCDS images reveal a clear three-zone concentric pattern [Fig. 4(m, n)]. Similarly, aLIV and LIV exhibit a concentric pattern of low (red)–moderate (yellow with red dots)–high (green) zones from the inner to outer regions [Fig. 4(k, l)]. In the innermost zone, a very small proportion of scatterers are dynamic (low aLIV and LIV) and move at high speed (high Swiftness). In the middle zone, both static and dynamic scatterers coexist (moderate aLIV and LIV), with dynamic scatterers moving at slower speeds (low Swiftness) within the fingerprint speed zone of OCDS (high OCDS). The outermost zone of the aLIV and LIV images resembles the outer zone of the without-drug and 1-day-treated spheroids, namely, a large proportion of the scatterers are dynamic (high aLIV and LIV). However, Swiftness and OCDS exhibit reverse contrasts to those of the without-drug and 1-day-treated spheroids. This indicates that the dynamic scatterers move rapidly (high Swiftness) and their speed is outside the fingerprint speed zone of OCDS (low OCDS). It is noteworthy that the fluorescence image does not differentiate the three concentric zones because the living and dead cells are intermixed.

For the 6-day-treated spheroid, aLIV and LIV indicate that a very small proportion of scatterers are dynamic (low aLIV and LIV) across the entire spheroid [Fig. 4(p, q)]. However, Swiftness reveals a tessellated pattern, with some domains containing fast-moving scatterers and others containing slow-moving scatterers [Fig. 4(r)]. A similar tessellated pattern is evident in the OCDS image [Fig. 4(s)]. The fluorescence image also shows a similar tessellated pattern of dead and living cell domains [Fig. 4(t)].

Figure 5 shows the *en face* and B-scan aLIV, LIV, Swiftness, and OCDS images of the *ex vivo* mouse kidney. Similar to the characteristics reported by Mukherjee *et al.* [33], pipe-like structures with a large proportion of dynamic scatterers (high aLIV and LIV) can be observed in the inner region of the kidney in the *en face* images [Fig. 5(a, b)]. The low Swiftness and low OCDS values indicate that the dynamic scatterers in these structure move slowly (low Swiftness) and their speed is within the fingerprint speed zone of OCDS (high OCDS) [Fig. 5(c, d)].

Vertical stripes appear in the B-scan images [Fig. 5(e–h)]. Mukherjee *et al.* investigated the LIV of mouse kidneys, and hypothesized that the vertical stripes of high LIV are artifacts caused by fast motion at the upper-most part of the stripes [33]. However, this hypothesis was not confirmed in that study because only LIV was used for DOCT imaging in Ref. [33]. On the other

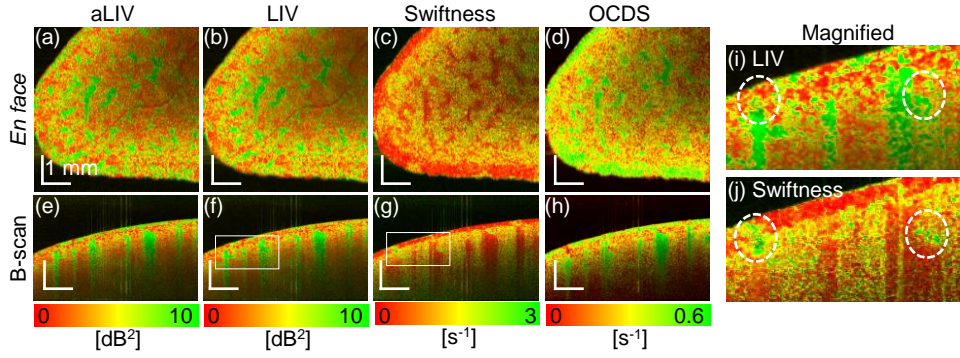


Fig. 5. The *en face* and B-scan aLIV, LIV, Swiftness, and OCDS images of the *ex vivo* mouse kidney. The scale bars represent 1 mm. The magnified images of LIV and Swiftness (i, j) correspond to the square regions in the B-scan images (f, g), respectively. Several pipe-like structures are visible, and they exhibit high aLIV values, which may indicate high occupancy of dynamic scatterers (high dynamic scatterer ratio), and low Swiftness values, suggesting the motion of the dynamic scatterers is slow.

hand, the Swiftness image obtained in the present study provides supporting evidence. Namely, at the top of the vertical stripes [dotted circles in Fig. 5(i, j), which are magnified images of the square regions in Fig. 5(f, g)], high Swiftness values are observed, indicating high-speed dynamic scatterers. These regions exhibit low OCDS, probably because the scatterer speeds exceed the fingerprint speed zone of OCDS.

4.2.2. Study 2

Figure 6(a–d) presents the $\mathcal{V}A_{tw}$ (virtual acquisition time window) dependency of each DOCT metric. Specifically, Fig. 6(a–c) shows the mean DOCT values of aLIV and LIV [Fig. 6(a)], Swiftness [Fig. 6(b)], and OCDS [Fig. 6(c)] at the two ROIs. The core and periphery ROIs used for the analysis are indicated in Fig. 6(e).

Here we note that the DOCT values might be more faithful with larger $\mathcal{V}A_{tw}$ values because the larger $\mathcal{V}A_{tw}$ correspond to longer acquisition time duration and greater number of time points. All DOCT metrics exhibit a clear dependency on $\mathcal{V}A_{tw}$. Specifically, as $\mathcal{V}A_{tw}$ becomes smaller, aLIV, LIV, and OCDS decrease while Swiftness increases.

The contrast of each DOCT metric between the core and periphery ROIs is plotted in Fig. 6(d). The OCDS of the core ROI exhibits erroneous negative values for small $\mathcal{V}A_{tw}$ values, thus, the contrast of the OCDS was not computed. These erroneous values may be caused by the limited number of time points involved in the OCDS computation. For aLIV, LIV, and Swiftness, the contrast becomes large and stable as $\mathcal{V}A_{tw}$ increases. It appears that aLIV stabilize faster than LIV. Considering that the DOCT values are more reliable at larger $\mathcal{V}A_{tw}$, aLIV might be a more reliable metric than LIV.

The contrast between the core and periphery ROIs for aLIV, LIV, and Swiftness decreases monotonically as $\mathcal{V}A_{tw}$ becomes smaller [Fig. 6(d)]. The aLIV metric demonstrates higher contrast than LIV, except at $\mathcal{V}A_{tw} = 0.41$ s. This higher contrast of aLIV agrees with our expectations based on the principle of aLIV. Namely, the saturation speed of the LIV curve is slow and it does not reach the saturation level within A_{tw} , such as in the case of the periphery ROI, the aLIV value, which is the expected saturation level of the curve, becomes larger than the LIV values. On the other hand, if the LIV curve saturates fast, such as in the case of core ROI, the aLIV and LIV values become close to each other. And hence, the contrast of aLIV between two ROIs can be higher than that of LIV, especially A_{tw} is small. Note that the case of

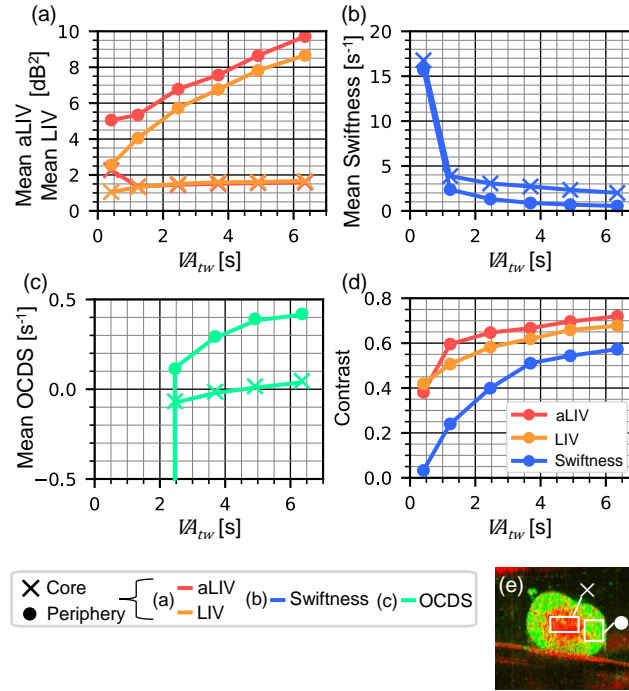


Fig. 6. (a, b, c) Mean DOCT values in each core (x) and periphery (●) ROI of the spheroids. (d) Contrast between core and periphery ROIs. The two ROIs were manually defined as shown by the squares in (e).

the shortest A_{tw} (0.41 s) is an exception, where the A_{tw} is too short to correctly estimate the saturation level (that is the aLIV).

Figure 7 shows B-scan images of aLIV, LIV, Swiftness, and OCDS of a tumor spheroid at each \overline{VA}_{tw} . The observational contrasts are consistent with the contrast plot of Fig. 6. The image quality of all DOCT metrics degrades as \overline{VA}_{tw} decreases. According to subjective observations, the image quality of aLIV and LIV with $\overline{VA}_{tw} = 3.69$ s or larger is acceptable. In the Swiftness image, the spheroid core is distinguishable for $\overline{VA}_{tw} = 1.23$ s or larger, while for OCDS, the core is distinguishable for $\overline{VA}_{tw} = 2.46$ s or larger.

Figure 8 shows B-scan images of aLIV, LIV, Swiftness, and OCDS for the mouse kidney at each \overline{VA}_{tw} . The DOCT images of the mouse kidney exhibit a similar \overline{VA}_{tw} dependency as observed for the spheroid.

5. Discussion

5.1. DOCT signals and intratissue/intracellular motions

Most of the DOCT algorithms are not direct measures of sample dynamics (i.e., intratissue and intracellular motions) but measures of OCT signal fluctuations. In general, complex OCT signal is expressed as a summation of phasor contributions from scatterers in the tissue. The time frequency of the complex OCT sequence may directly correspond to the vibration of the phasors, but the vibration frequency of a phasor does not necessarily equal the vibration frequency of the scatterers. It can be easily imagined that the phase of the phasor rotates even when the scatterer moves with constant linear motion. Furthermore, several Fourier-spectrum-based DOCT methods use the time-frequency spectrum of the intensity or amplitude OCT signal sequence [21–26].

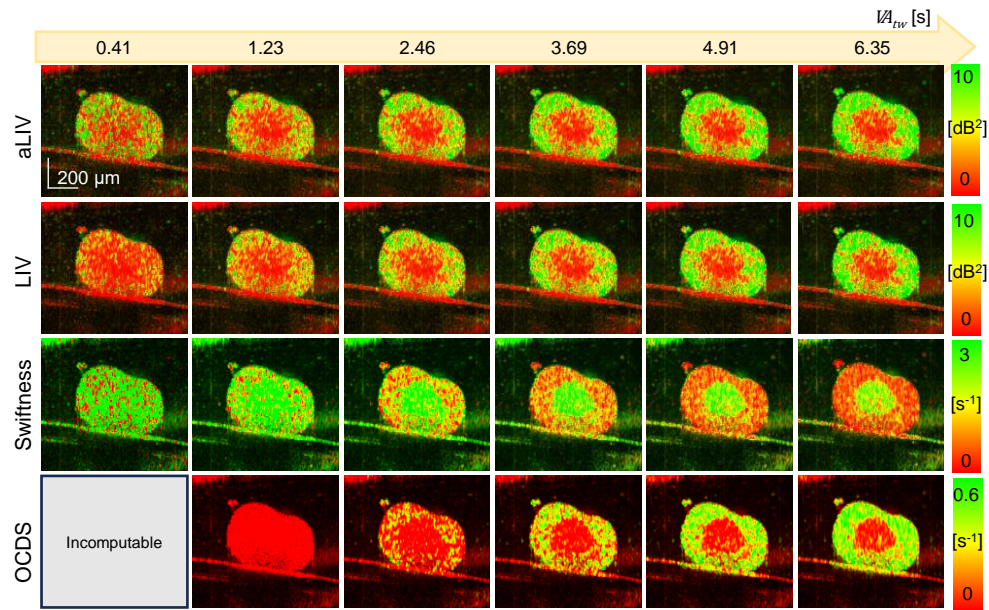


Fig. 7. Image quality comparison of aLIV, LIV, Swiftness, and OCDS for several VA_{TW} values. The original data is that of the without-drug spheroid in Fig. 4.

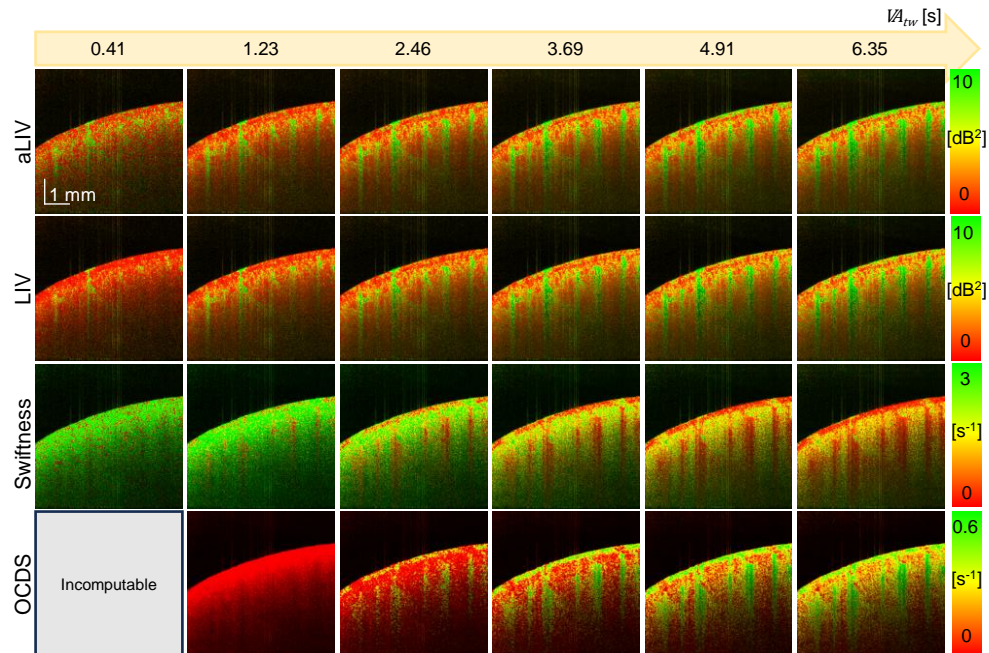


Fig. 8. Image quality comparison of aLIV, LIV, Swiftness, and OCDS for each VA_{TW} . The original data is that of the mouse kidney in Fig. 5.

According to discrete-scatterer-based formulations of OCT [35,48], the intensity of OCT consists of interaction terms (i.e., the multiplications) of the phasors (see Section 3.2 and Fig. 2 of Ref. [35]). These interactions generate new frequency components that were not in the original complex OCT sequence. And hence, the Fourier-spectrum-based DOCT contrasts are not really direct measures of the sample motion. Note that, since OCT amplitude is defined as the square root of intensity, amplitude-based methods are also not free from this issue. (Note that the Taylor series expansion of the square root may have infinitely high order terms.)

Similarly, autocorrelation-based methods [12, 15, 17] are also not really direct measures of sample dynamics. It can be understood from the fact that the autocorrelation function and the power spectrum are tightly related by Wiener-Khinchin theorem. Note that, among the autocorrelation-based methods, OCDS [17] uses logarithmic intensity, and the Taylor series expansion of the logarithmic function also consists infinitely high order terms. And hence, OCDS is also not a direct measure of the sample dynamics.

Our new DOCT metrics, i.e., aLIV and Swiftness, are also not free from this issue. However, the numerical analyses revealed relatively straightforward relationships between these metrics and the sample dynamics (Section 3). Namely, aLIV mainly corresponds to DSR, while Swiftness mainly corresponds to the scatterer speed. These simple relationships enable easy interpretation of DOCT images. In addition, these properties of aLIV and Swiftness will also enable quantitative measurement of DSR and scatterer speed by combining with a sophisticated estimation theory as shown in a preliminary demonstration [49].

5.2. Ambiguous LIV curve and unreliable aLIV and Swiftness values

There are two types of LIV curves that inevitably lead to unreliable parameter fitting, and hence produce unreliable aLIV and Swiftness values.

The first such LIV curve, referred to as Type-A ambiguous LIV curve, constantly takes values close to 0 dB² regardless of T_w (the time window of the variance computation). This type of LIV curve corresponds to the case in which there are almost no dynamic scatterers. In this case, myriad (a, τ) -pairs of Eq. (3) provide a solution to the curve fitting. Namely, if a is zero, any value of τ gives a solution. Similarly, if τ approaches ∞ , any value of a can be a solution. Hence, aLIV and Swiftness are not definitive with this type of LIV curve.

The second unreliable LIV curve, referred to as Type-B ambiguous LIV curve, is characterized by its monotonic increase with respect to T_w without becoming saturated, namely, the true τ (i.e., the true time constant) is significantly larger than the maximum acquisition time A_{T_w} . This type of LIV curve corresponds to the case in which the dynamic scatterers move very slowly. In this case, the fitting algorithm needs to predict the saturation level a that the curve may reach outside of the fitting range. Namely, the algorithm needs to extrapolate the data sequence, which causes instability and inaccuracy of fitting, and hence, produce unreliable aLIV and Swiftness values.

Although these two types of LIV curves cause unreliable aLIV and Swiftness computations, they can be automatically detected and removed from quantitative analyses. The Type-A ambiguous LIV curve is characterized by persistent small values around zero, and hence can be detected by the following criterion:

$$\sqrt{\langle \overline{\text{LIV}}^2(T_w) \rangle_{T_w}} \leq 2 \sqrt{\langle (\overline{\text{LIV}}(T_w) - f_{\text{LIV}}(T_w; a, \tau))^2 \rangle_{T_w}}, \quad (13)$$

where $\langle \cdot \rangle_{T_w}$ represents averaging over T_w , $\overline{\text{LIV}}(T_w)$ is the LIV curve, and $f_{\text{LIV}}(T_w; a, \tau)$ is the estimated first-order saturation function. Namely, if the root-mean-square of the LIV curve is less than twice the root-mean-square-error of the fitting, $\overline{\text{LIV}}(T_w)$ is considered to be constantly zero and the curve is classified to be a Type-A ambiguous LIV curve.

The Type-B ambiguous LIV curve corresponds to the case in which the time constant τ is far

larger than the maximum acquisition time A_{tw} . This can be detected by the following criterion:

$$\tau \geq 2A_{tw}. \quad (14)$$

Namely, if the estimated time constant τ is greater than twice the maximum acquisition time, the curve is considered to be a Type-B ambiguous LIV curve.

Occurrences of the two types of ambiguous LIV curves were examined using the experimentally obtained datasets of Section 4. The ambiguous LIV curves were detected by Eqs. (13) and (14), and the occurrences were computed within the tissue region selected by an empirical intensity threshold. Table 1 summarizes the mean and standard deviation of the occurrences among the five datasets (i.e., four spheroids and mouse kidney). The numbers in the table denote the percentage of curves (i.e., pixels in the aLIV and Swiftness images) of each types. On average, more than 97% of the LIV curves are classified as unambiguous (i.e., neither Type-A nor Type-B). Namely, more than 97% of the pixels in the aLIV and Swiftness images are unambiguous.

Table 1. Occurrence of ambiguous LIV curves with in the tissue region. Each cell indicates the mean and standard deviation of the percent-occurrences among five samples. The results indicate that more than 97% of pixels in the tissue regions are unambiguous.

	Type-A	Not Type-A
Type-B	$0.24 \times 10^{-3} \pm 0.53 \times 10^{-3} \%$	$2.24 \pm 0.91 \%$
Not Type-B	$0.00 \pm 0.00 \%$	$97.76 \pm 0.91 \%$

The impact of exclusion of the unreliable pixels caused by ambiguous LIV curves is now examined using the spheroid dataset without drug administration. The means and standard deviations of aLIV and Swiftness in the core and periphery ROIs were computed with (w/) and without (w/o) unreliable pixels, and the results are summarized in Table 2.

Table 2. Mean \pm standard deviation of aLIV and Swiftness values at two ROIs with (w/) and without (w/o) unreliable pixels.

	Unreliable pixels	aLIV [dB ²]	Swiftness [s ⁻¹]
Core ROI	w/	1.58 ± 1.40	2.00 ± 0.688
	w/o	1.58 ± 1.40	2.00 ± 0.688
Periphery ROI	w/	$12.1 \times 10^3 \pm 192 \times 10^3$	0.517 ± 0.304
	w/o	9.71 ± 6.52	0.543 ± 0.290

The exclusion of unreliable pixels results in a marked reduction in the mean aLIV value in the periphery ROI. Our specific curve fitting algorithm tends to give very high estimate of a if it is ambiguous, and it causes the very high mean aLIV value. This result suggests that the exclusion of unreliable pixels is essential when using the DOCT metrics for quantitative analyses.

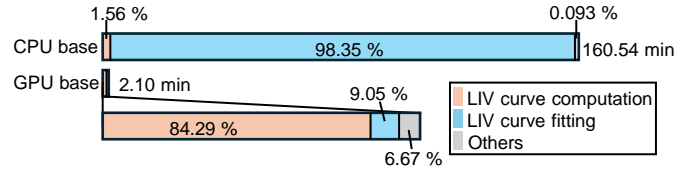


Fig. 9. Processing time of aLIV and Swiftsness by the CPU- and GPU-based fitting methods. The total processing time by the GPU-based method is approximately 2.10 min, which is 76.44 times faster than the CPU-based method. The total processing time includes LIV curve computation, LIV curve fitting, and other minor processes.

5.3. Processing time of aLIV and Swiftsness

In our DOCT imaging, volumetric time-sequential OCT data were acquired under the following configurations: 128 locations per single volume, 32 frames per B-scan location, and 512×402 pixels per frame. The total processing time for computing aLIV and Swiftsness (excluding standard OCT signal reconstruction) for a volume was approximately 2.10 min in our GPU-based environment (described in Section 2.3) excluding the hard-disk access time. As summarized in Fig. 9, the computation of the LIV curve and the LIV curve fitting accounted for 84.29% and 9.05% of the total processing time, respectively.

The LIV curve fitting was implemented using the GPU-based fitting method “`gf.fit_constrained()`” in the Gpufit library [37]. To evaluate the necessity for GPU-based processing, the GPU-based fitting method was compared with a CPU-based fitting method, namely “`scipy.optimize.curve_fit()`” in the SciPy 1.5.2 library. The model function, algorithm, and parameter exploration range were identical to those in the GPU based method.

The total processing time for aLIV and Swiftsness using the CPU-based fitting method was approximately 160.54 min. The processing times for LIV curve fitting were 0.19 min and 157.89 min for the GPU- and CPU-based fitting methods, respectively. This verification confirms that the GPU-based fitting method accelerates the LIV curve fitting by a factor of 831.0.

5.4. Current and future validations of DOCT

Experimental validation of DOCT methods using dynamic phantoms is important. However, dynamic phantoms with known and well-controlled dynamics have not yet been established. Although scatterer suspensions can be used as phantoms to model diffusion motion, diffusion alone does not accurately represent the dominant motion in cells [50]. As a result, experimental quantitative validation remains challenging. Alternatively, we validated the DOCT algorithms through simulations using a numerical sample model, which can be regarded a well-controlled numerical phantom.

Apart from the phantom-based validation, comparing DOCT images with established tissue and cell imaging techniques, such as histology and fluorescence microscopy, is also important. In this study, we compared DOCT images of spheroids with standard and well-established live/dead fluorescence micrographs (Fig. 4), which significantly aided the interpretation of DOCT images. However, such a comparison has not yet been conducted for *ex vivo* kidney samples. Although a detailed interpretation of kidney dynamics is beyond the scope of this paper, such comparisons will contribute to a more comprehensive understanding of DOCT images of the kidney in future studies.

5.5. Numerical investigation for more complicated scatterer dynamics

In our numerical simulations, we assumed that active transport and cyclosis within the cells are the dominant intratissue activities, and modeled these activities using the random ballistic motion model (Section 3.1.1). However, to comprehensively examine all intratissue activities, a more complex model is necessary. It has been known that various types of intratissue activities occur on different time scales [51]. Consequently, the random ballistic motion model may not represent all types of intratissue activities.

Feng *et al.* expanded the modeling of intratissue scatterer motions by introducing mono-directional displacement (flow) and diffusion (Brownian) motion models, in addition to the random ballistic motion model [39]. This comprehensive set of motion models may enable the DOCT metrics to be interpreted for a wide spectrum of sample types beyond cellular samples, such as those exhibiting cellular migration and flow, and more aqueous samples.

6. Conclusion

In this paper, we proposed a new DOCT algorithm. By leveraging the A_{tw} -size dependency of LIV, two DOCT metrics, named aLIV and Swiftness, were derived. Numerical simulations revealed that aLIV is sensitive to the occupancy of dynamic scatterers (dynamic scatterer ratio), whereas Swiftness is sensitive to the speed of the dynamic scatterers. Experimental validations using *in vitro* tumor spheroids and an *ex vivo* mouse kidney demonstrated that aLIV and Swiftness images provide more direct insights into the intratissue activities than our conventional DOCT metrics.

Bolstered by numerical-simulation-based interpretation, the multiple DOCT metrics will enhance the utility and applications of DOCT imaging.

Funding

Core Research for Evolutional Science and Technology (JPMJCR2105); Japan Society for the Promotion of Science (21H01836, 22F22355, 22KF0058, 22K04962, 24KJ0510).

Disclosures

Morishita, Mukherjee, El-Sadek, Makita, Yasuno: Sky Technology(F), Nikon(F), Kao Corp.(F), Topcon(F), Panasonic(F), Santec (F). Seesan, Mori, Furukawa, Matsusaka, Fukuda, Lukmanto: None.

Data availability

The data that support the findings of this study are available from the corresponding author upon reasonable request. The new DOCT algorithms and the DOCT simulation framework are available as open-source Python library at Refs. [36] and [38], respectively.

References

1. D. Huang, E. A. Swanson, C. P. Lin, J. S. Schuman, W. G. Stinson, W. Chang, M. R. Hee, T. Flotte, K. Gregory, C. A. Puliafito, and J. G. Fujimoto, "Optical coherence tomography," *Science* **254**, 1178–1181 (1991).
2. J. A. Izatt, E. A. Swanson, J. G. Fujimoto, M. R. Hee, and G. M. Owen, "Optical coherence microscopy in scattering media," *Opt. Lett.* **19**, 590 (1994).
3. E. Beaurepaire, A. C. Boccara, M. Lebec, L. Blanchot, and H. Saint-Jalmes, "Full-field optical coherence microscopy," *Opt. Lett.* **23**, 244 (1998).
4. W. Drexler, U. Morgner, F. X. Kärtner, C. Pitris, S. A. Boppart, X. D. Li, E. P. Ippen, and J. G. Fujimoto, "In vivo ultrahigh-resolution optical coherence tomography," *Opt. Lett.* **24**, 1221 (1999).
5. A. Dubois, K. Grieve, G. Moneron, R. Lecaque, L. Vabre, and C. Boccara, "Ultrahigh-resolution full-field optical coherence tomography," *Appl. Opt.* **43**, 2874 (2004).
6. A. D. Aguirre, C. Zhou, H.-C. Lee, O. O. Ahsen, and J. G. Fujimoto, *Optical coherence microscopy* (Springer International Publishing, Cham, 2015), chap. 28, pp. 865–911.

7. Y. Huang, J. Zou, M. Badar, J. Liu, W. Shi, S. Wang, Q. Guo, X. Wang, S. Kessel, L. L.-Y. Chan, P. Li, Y. Liu, J. Qiu, and C. Zhou, "Longitudinal morphological and physiological monitoring of three-dimensional tumor spheroids using optical coherence tomography," *J. Vis. Exp.* (2019).
8. S.-E. Lin, D.-Y. Jheng, K.-Y. Hsu, Y.-R. Liu, W.-H. Huang, H.-C. Lee, and C.-C. Tsai, "Rapid pseudo-H&E imaging using a fluorescence-inbuilt optical coherence microscopic imaging system," *Biomed. Opt. Express* **12**, 5139 (2021).
9. Y. Ming, S. Hao, F. Wang, Y. R. Lewis-Israeli, B. D. Volmert, Z. Xu, A. Goestenkors, A. Aguirre, and C. Zhou, "Longitudinal morphological and functional characterization of human heart organoids using optical coherence tomography," *Biosens. Bioelectron.* **207**, 114136 (2022).
10. K. Chen, W. Song, L. Han, and K. Bizheva, "Powell lens-based line-field spectral domain optical coherence tomography system for cellular resolution imaging of biological tissue," *Biomed. Opt. Express* **14**, 2003 (2023).
11. K. Chen, N. Abbasi, A. Wong, and K. Bizheva, "In vivo, contactless, cellular resolution imaging of the human cornea with Powell lens based line field OCT," *Sci. Rep.* **14** (2024).
12. C. Apelian, F. Harms, O. Thouvenin, and A. C. Boccara, "Dynamic full field optical coherence tomography: subcellular metabolic contrast revealed in tissues by interferometric signals temporal analysis," *Biomed. Opt. Express* **7**, 1511 (2016).
13. C. Ren, S. Hao, F. Wang, A. Matt, M. M. Amaral, D. Yang, L. Wang, and C. Zhou, "Dynamic contrast optical coherence tomography (DyC-OCT) for label-free live cell imaging," *Commun. Biol.* **7** (2024).
14. A. L. Oldenburg, R. K. Chhetri, D. B. Hill, and B. Button, "Monitoring airway mucus flow and ciliary activity with optical coherence tomography," *Biomed. Opt. Express* **3**, 1978 (2012).
15. A. L. Oldenburg, X. Yu, T. Gilliss, O. Alabi, R. M. Taylor, and M. A. Troester, "Inverse-power-law behavior of cellular motility reveals stromal-epithelial cell interactions in 3D co-culture by OCT fluctuation spectroscopy," *Optica* **2**, 877 (2015).
16. O. Thouvenin, M. Fink, and A. C. Boccara, "Dynamic multimodal full-field optical coherence tomography and fluorescence structured illumination microscopy," *J. Biomed. Opt.* **22**, 1 (2017).
17. I. Abd El-Sadek, A. Miyazawa, L. Tzu-Wei Shen, S. Makita, S. Fukuda, T. Yamashita, Y. Oka, P. Mukherjee, S. Matsusaka, T. Oshika, H. Kano, and Y. Yasuno, "Optical coherence tomography-based tissue dynamics imaging for longitudinal and drug response evaluation of tumor spheroids," *Biomed. Opt. Express* **11**, 6231 (2020).
18. S. Park, T. Nguyen, E. Benoit, D. L. Sackett, M. Garmendia-Cedillos, R. Pursley, C. Boccara, and A. Gandjbakhche, "Quantitative evaluation of the dynamic activity of HeLa cells in different viability states using dynamic full-field optical coherence microscopy," *Biomed. Opt. Express* **12**, 6431 (2021).
19. J. Scholler, "Motion artifact removal and signal enhancement to achieve in vivo dynamic full field OCT," *Opt. Express* **27**, 19562 (2019).
20. K. Fei, Z. Luo, Y. Chen, Y. Huang, S. Li, V. Mazlin, A. C. Boccara, J. Yuan, and P. Xiao, "Cellular structural and functional imaging of donor and pathological corneas with label-free dual-mode full-field optical coherence tomography," *Biomed. Opt. Express* **15**, 3869 (2024).
21. Y. Ling, X. Yao, U. A. Gamm, E. Arteaga-Solis, C. W. Emala, M. A. Choma, and C. P. Hendon, "Ex vivo visualization of human ciliated epithelium and quantitative analysis of induced flow dynamics by using optical coherence tomography," *Lasers Surg. Med.* **49**, 270–279 (2017).
22. O. Thouvenin, C. Boccara, M. Fink, J. Sahel, M. Pâques, and K. Grieve, "Cell motility as contrast agent in retinal explant imaging with full-field optical coherence tomography," *Invest. Ophthalmol. Vis. Sci.* **58**, 4605 (2017).
23. M. Münter, M. vom Endt, M. Pieper, M. Casper, M. Ahrens, T. Kohlfaerber, R. Rahmanzadeh, P. König, G. Hüttmann, and H. Schulz-Hildebrandt, "Dynamic contrast in scanning microscopic OCT," *Opt. Lett.* **45**, 4766 (2020).
24. H. M. Leung, M. L. Wang, H. Osman, E. Abouei, C. MacAulay, M. Follen, J. A. Gardecki, and G. J. Tearney, "Imaging intracellular motion with dynamic micro-optical coherence tomography," *Biomed. Opt. Express* **11**, 2768 (2020).
25. T. Xia, K. Umezu, D. M. Scully, S. Wang, and I. V. Larina, "In vivo volumetric depth-resolved imaging of cilia metachronal waves using dynamic optical coherence tomography," *Optica* **10**, 1439 (2023).
26. K. Chen, S. Swanson, and K. Bizheva, "Line-field dynamic optical coherence tomography platform for volumetric assessment of biological tissues," *Biomed. Opt. Express* **15**, 4162 (2024).
27. I. A. El-Sadek, A. Miyazawa, L. T.-W. Shen, S. Makita, P. Mukherjee, A. Lichtenegger, S. Matsusaka, and Y. Yasuno, "Three-dimensional dynamics optical coherence tomography for tumor spheroid evaluation," *Biomed. Opt. Express* **12**, 6844 (2021).
28. I. Abd El-Sadek, L. T.-W. Shen, T. Mori, S. Makita, P. Mukherjee, A. Lichtenegger, S. Matsusaka, and Y. Yasuno, "Label-free drug response evaluation of human derived tumor spheroids using three-dimensional dynamic optical coherence tomography," *Sci. Rep.* **13** (2023).
29. I. Abd El-Sadek, R. Morishita, T. Mori, S. Makita, P. Mukherjee, S. Matsusaka, and Y. Yasuno, "Label-free visualization and quantification of the drug-type-dependent response of tumor spheroids by dynamic optical coherence tomography," *Sci. Rep.* **14** (2024).
30. R. Morishita, T. Suzuki, P. Mukherjee, I. Abd El-Sadek, Y. Lim, A. Lichtenegger, S. Makita, K. Tomita, Y. Yamamoto, T. Nagamoto, and Y. Yasuno, "Label-free intratissue activity imaging of alveolar organoids with dynamic optical coherence tomography," *Biomed. Opt. Express* **14**, 2333 (2023).
31. P. Mukherjee, A. Miyazawa, S. Fukuda, T. Yamashita, D. Lukmanto, K. Okada, I. A. El-Sadek, L. Zhu, S. Makita, T. Oshika, and Y. Yasuno, "Label-free functional and structural imaging of liver microvascular complex in mice by

- Jones matrix optical coherence tomography,” *Sci. Rep.* **11** (2021).
32. P. Mukherjee, S. Fukuda, D. Lukmanto, T. Yamashita, K. Okada, S. Makita, I. Abd El-Sadek, A. Miyazawa, L. Zhu, R. Morishita, A. Lichtenegger, T. Oshika, and Y. Yasuno, “Label-free metabolic imaging of non-alcoholic-fatty-liver-disease (NAFLD) liver by volumetric dynamic optical coherence tomography,” *Biomed. Opt. Express* **13**, 4071 (2022).
 33. P. Mukherjee, S. Fukuda, D. Lukmanto, T. H. Tran, K. Okada, S. Makita, I. A. El-Sadek, Y. Lim, and Y. Yasuno, “Renal tubular function and morphology revealed in kidney without labeling using three-dimensional dynamic optical coherence tomography,” *Sci. Rep.* **13** (2023).
 34. Y. Guo, R. Morishita, I. Abd El-Sadek, P. Mukherjee, Y. Zhu, and Y. Yasuno, “In vivo dynamic optical coherence tomography with hardware- and software-based motion correction,” in *Optical Coherence Tomography and Coherence Domain Optical Methods in Biomedicine XXVIII*, J. A. Izatt and J. G. Fujimoto, eds. (SPIE, 2024).
 35. K. Tomita, S. Makita, N. Fukutake, R. Morishita, I. Abd El-Sadek, P. Mukherjee, A. Lichtenegger, J. Tamaoki, L. Bian, M. Kobayashi, T. Mori, S. Matsusaka, and Y. Yasuno, “Theoretical model for en face optical coherence tomography imaging and its application to volumetric differential contrast imaging,” *Biomed. Opt. Express* **14**, 3100 (2023).
 36. Computational optics group at the University of Tsukuba, “Dynamic-optical-coherence-tomography contrast-generation library by computational optics group,” Open source GitHub repository (2025). <https://github.com/ComputationalOpticsGroup/COG-dynamic-OCT-contrast-generation-library>.
 37. A. Przybylski, B. Thiel, J. Keller-Findeisen, B. Stock, and M. Bates, “Gpufit: An open-source toolkit for GPU-accelerated curve fitting,” *Sci. Rep.* **7** (2017).
 38. Computational optics group at the University of Tsukuba, “Dynamic-optical-coherence-tomography simulation library by computational optics group,” Open source GitHub repository (2025). <https://github.com/ComputationalOpticsGroup/COG-dynamic-OCT-contrast-simulation-library>.
 39. Y. Feng, S. Fujimura, Y. Lim, T. Seesan, R. Morishita, I. Abd El-Sadek, P. Mukherjee, and Y. Yasuno, “Mathematical modeling of intracellular and intratissue activities for understanding dynamic optical coherence tomography signals,” in *Optical Coherence Tomography and Coherence Domain Optical Methods in Biomedicine XXVIII*, (Proc. SPIE, 2024), p. PC128300H.
 40. R. F. Spaide, J. G. Fujimoto, and N. K. Waheed, “Image artifacts in optical coherence tomography angiography,” *Retina* **35**, 2163–2180 (2015).
 41. D. D. Nolte, “Coherent light scattering from cellular dynamics in living tissues,” *Reports on Prog. Phys.* **87**, 036601 (2024).
 42. T. Seesan, I. Abd El-Sadek, P. Mukherjee, L. Zhu, K. Oikawa, A. Miyazawa, L. T.-W. Shen, S. Matsusaka, P. Buranasiri, S. Makita, and Y. Yasuno, “Deep convolutional neural network-based scatterer density and resolution estimators in optical coherence tomography,” *Biomed. Opt. Express* **13**, 168 (2021).
 43. T. Seesan, P. Mukherjee, I. A. El-Sadek, Y. Lim, L. Zhu, S. Makita, and Y. Yasuno, “Optical-coherence-tomography-based deep-learning scatterer-density estimator using physically accurate noise model,” *Biomed. Opt. Express* **15**, 2832–2848 (2024).
 44. S. Fujimura, I. Abd El-Sadek, P. Mukherjee, Y. Lim, L. Zhu, R. Morishita, Y. Feng, and Y. Yasuno, “Investigating the dependency of dynamic optical coherence tomography signals on resolution and wavelength by experimental and simulation approaches,” in *Optical Coherence Tomography and Coherence Domain Optical Methods in Biomedicine XXVIII*, (Proc. SPIE, 2024), p. PC128301E.
 45. E. Li, S. Makita, Y.-J. Hong, D. Kasaragod, and Y. Yasuno, “Three-dimensional multi-contrast imaging of *in vivo* human skin by Jones matrix optical coherence tomography,” *Biomed. Opt. Express* **8**, 1290 (2017).
 46. A. Miyazawa, S. Makita, E. Li, K. Yamazaki, M. Kobayashi, S. Sakai, and Y. Yasuno, “Polarization-sensitive optical coherence elastography,” *Biomed. Opt. Express* **10**, 5162 (2019).
 47. E. C. Costa, A. F. Moreira, D. de Melo-Diogo, V. M. Gaspar, M. P. Carvalho, and I. J. Correia, “3D tumor spheroids: an overview on the tools and techniques used for their analysis,” *Biotechnol. Adv.* **34**, 1427–1441 (2016).
 48. K. C. Zhou, R. Qian, A.-H. Dhalla, S. Farsi, and J. A. Izatt, “Unified k-space theory of optical coherence tomography,” *Adv. Opt. Photonics* **13**, 462 (2021).
 49. F. Shumpei, E.-S. Ibrahim, Abd, M. Rion, F. Yuanke, and Y. Yoshiaki, “Intracellular activity-type and parameter estimation from dynamic optical coherence tomography signals,” in *Optical Coherence Tomography and Coherence Domain Optical Methods in Biomedicine XXIX*, (Proc. SPIE, 2025).
 50. F. Yuanke, F. Shumpei, L. Yiheng, S. Thitiya, M. Rion, E.-S. Ibrahim, Abd, M. Pradipta, and Y. Yoshiaki, “Dynamic oct simulator based on mathematical models of intratissue dynamics, image formation, and measurement noise,” in *Optical Coherence Tomography and Coherence Domain Optical Methods in Biomedicine XXIX*, (Proc. SPIE, 2025).
 51. J. A. Papin, T. Hunter, B. O. Palsson, and S. Subramaniam, “Reconstruction of cellular signalling networks and analysis of their properties,” *Nat. Rev. Mol. Cell Biol.* **6**, 99–111 (2005).

Supplementary Material

S1. Analytic field of numerical simulation

Figure S1 schematically show the analytic field size for x direction.

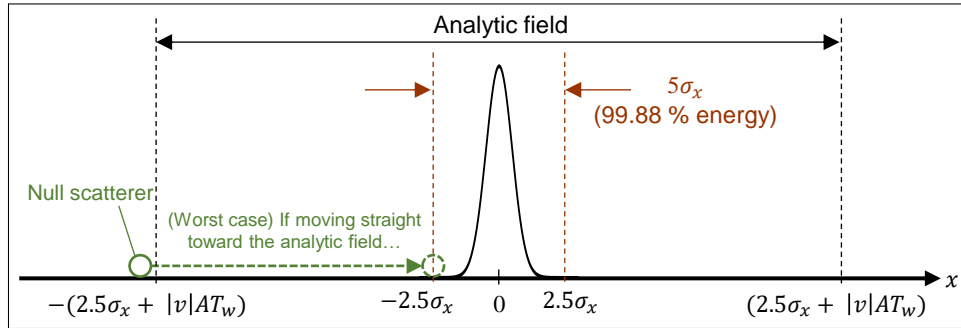


Fig. S1. Schematic depiction of the analytic field size and complex PSF for x direction.

S2. Terminology

The terminology and abbreviations used in this paper are summarized in Table S1.

Table S1. Terminology and abbreviations.

Abbreviation	Meaning
DOCT	Dynamic optical coherence tomography
A_{tw}	Acquisition time window of full data
T_w	Time window of data subset to compute LIV
\tilde{A}_{tw}	Acquisition time window for virtual frame-decreased data
LIV	Logarithmic intensity variance
OCDS	OCT correlation decay speed
aLIV	Authentic LIV
LIV curve	Sequential LIV over T_w at a single location
a	Saturation level; first fitting parameter
τ	Time constant; second fitting parameter
PSF	Point spread function
FOV	Field of view
PTX	Paclitaxel; one type of anti-cancer drugs
DSR	Dynamic-scatterer ratio
ROI	Region of interest